

Vortex dynamics in the two-dimensional BCS-BEC crossover

Received: 12 January 2022

Accepted: 3 November 2022

Published online: 16 November 2022



Max Heyl^{1,2,9}, Kyosuke Adachi^{3,4,9}, Yuki M. Itahashi¹, Yuji Nakagawa¹,
Yuichi Kasahara⁵, Emil J. W. List-Kratochvil^{2,6}, Yusuke Kato⁷ &
Yoshihiro Iwasa^{1,8} ✉

The Bardeen–Cooper–Schrieffer (BCS) condensation and Bose–Einstein condensation (BEC) are the two limiting ground states of paired Fermion systems, and the crossover between these two limits has been a source of excitement for both fields of high temperature superconductivity and cold atom superfluidity. For superconductors, ultra-low doping systems like graphene and Li_xZrNCl successfully approached the crossover starting from the BCS-side. These superconductors offer new opportunities to clarify the nature of charged-particles transport towards the BEC regime. Here we report the study of vortex dynamics within the crossover using their Hall effect as a probe in Li_xZrNCl . We observed a systematic enhancement of the Hall angle towards the BCS-BEC crossover, which was qualitatively reproduced by the phenomenological time-dependent Ginzburg-Landau (TDGL) theory. Li_xZrNCl exhibits a band structure free from various electronic instabilities, allowing us to achieve a comprehensive understanding of the vortex Hall effect and thereby propose a global picture of vortex dynamics within the crossover. These results demonstrate that gate-controlled superconductors are ideal platforms towards investigations of unexplored properties in BEC superconductors.

The crossover between the two limiting ground states of Fermion systems—the BCS and BEC state—has attracted continuous interest both theoretically and experimentally from the communities of ultracold atomic gases and superconductors^{1–3}. The first experimental realization of the BCS-BEC crossover was achieved in ultracold atomic gases⁴ starting from the BEC side, while the approach with superconductors from the BCS side⁵ has become active since recent discoveries of suitable materials including FeSe ⁶, twisted graphene^{7,8}, and Li_xZrNCl ⁹. The two BCS-BEC crossover systems, twisted trilayer graphene and Li_xZrNCl , are highly two-dimensional (2D), and the carrier density can be controlled by a gate voltage. The tunable carrier density is highly advantageous to observe how the system evolves from the

BCS- to the BEC-limit. In fact, both systems approached the crossover regime by reducing the carrier density and reached $T_c/T_F=1/8$, where T_c and T_F are the critical temperature and the Fermi temperature, respectively. Since $T_c/T_F=1/8$ is the upper limit for 2D systems^{10,11} in the crossover, it confirms the successful approach of the 2D BCS-BEC crossover. By approaching the crossover towards the BEC-limit, the coupling strength described as the ratio of superconducting gap Δ to Fermi energy E_F increased⁹. One of the intriguing phenomena related to the enhancement of Δ/E_F is the dynamics of superconducting vortices. Figure 1a, b shows a comparison of the energy levels inside the vortices for the BEC and BCS limit. Inside the vortex core, the quasi-particle states are confined and quantized. According to the Caroli-de

¹Quantum-Phase Electronics Center and Department of Applied Physics, University of Tokyo, Tokyo, Japan. ²Department of Chemistry, Department of Physics & IRIS Adlershof, Humboldt-Universität zu Berlin, Zum Großen Windkanal 2, Berlin, Germany. ³Nonequilibrium Physics of Living Matter RIKEN Hakubi Research Team, RIKEN Center for Biosystems Dynamics Research, Kobe, Japan. ⁴RIKEN Interdisciplinary Theoretical and Mathematical Sciences Program, Wako, Japan. ⁵Department of Physics, Kyoto University, Kitashirakawa Oiwakecho, Kyoto, Japan. ⁶Helmholtz-Zentrum für Materialien und Energie GmbH, Hahn-Meitner-Platz 1, Berlin, Germany. ⁷Department of Basic Science, University of Tokyo, Tokyo, Japan. ⁸RIKEN, Center for Emergent Matter Science, Wako, Japan. ⁹These authors contributed equally: Max Heyl, Kyosuke Adachi. ✉e-mail: iwasa@ap.t.u-tokyo.ac.jp

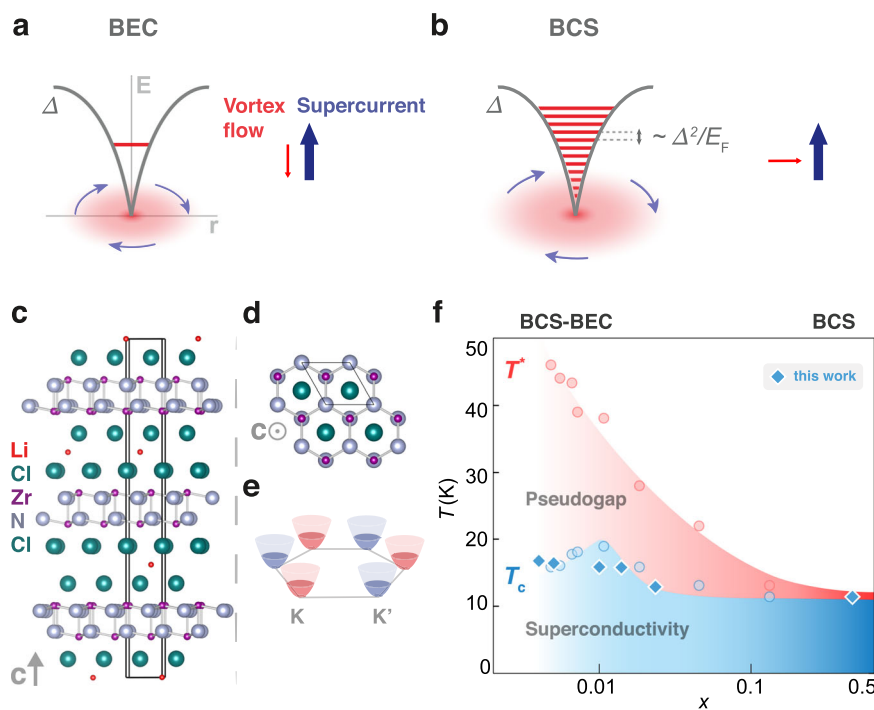


Fig. 1 | Properties of superconducting Li_xZrNCl . **a, b** Caroli-de Gennes-Matricone (CdGM) schematic of the quantized state(s) in the vortex core in the BEC **a** and BCS limit **b** are depicted. The vortex core is shaded in red, and the axis labels E and r correspond to energy and distance, respectively. The directions of supercurrent and vortex flow are indicated. In the BEC limit, the vortex motion is dissipationless and the vortex flow is nearly anti-parallel to the supercurrent, while in the BCS limit the vortex motion is nearly perpendicular to the supercurrent. **c** and **d** Side and top view of the Li_xZrNCl crystal structure. The solid black

lines represent the hexagonal unit cell. **e** Schematic of the simple parabolic conduction bands of Li_xZrNCl , located at the corners of the hexagonal Brillouin zone (K and K' points). **f** The BCS-BEC crossover phase diagram of Li_xZrNCl with data points from this work superimposed. T_c was determined by the temperature at which the resistance is half the normal state value at 30 K, which is close enough to the Berezinskii–Kosterlitz–Thouless transition for 2D superconductors⁹. The gap-opening temperature T^* was determined in the previous study⁹, and the regime between T_c and T^* forms the pseudo-gap state.

Genes-Matricone picture¹², the energy level spacing is in the order of Δ^2/E_F . In the BCS limit, Δ^2/E_F is so small that the energy spectrum is almost continuous (Fig. 1b), and thus the quasiparticles in the core are easily scattered, resulting in energy dissipative vortex motion. In the BEC limit, on the other hand, the energy level spacing is large enough to form a single quantized level¹³ (Fig. 1a). This large level spacing renders the vortex motion dissipationless since the quasiparticles in the core cannot be scattered. The above difference results in contrasting vortex motions: the vortex in the BCS regime moves perpendicularly to the net supercurrent (Fig. 1b, arrows), while the vortex in the BEC regime moves parallel to the superfluid velocity, i.e., anti-parallel to the net supercurrent (Fig. 1a, arrows). In the BEC regime, the motion of vortices antiparallel (parallel) to the background current density \mathbf{J} (superfluid velocity) can be understood as follows: The vortex motion in the presence of the magnetic field \mathbf{B} induces the macroscopic electric field $\mathbf{E} = \mathbf{B} \times \mathbf{v}_v$, where \mathbf{v}_v is the vortex velocity. In the absence of dissipation in the steady state, $\mathbf{E} = \mathbf{B} \times \mathbf{v}_v$ should be perpendicular to \mathbf{J} to avoid acceleration of the supercurrent. Thus $\mathbf{J} \parallel \mathbf{v}_v$ follows. Hence, the dissipationless nature of the vortex core in the BEC regime (Fig. 1a) brings about vortex flow parallel or antiparallel to the supercurrent flow. This vortex flow parallel to the supercurrent has never been observed experimentally, but in the case of superfluidity of charge neutral bosons of ^4He , the parallel vortex flow was nicely demonstrated in the movie of ref. 14 (for more details on the analogy between single vortex dynamics and charged particle dynamics see Supplementary Note 1).

In superfluid ^4He , the vortex motion is parallel to the superfluid velocity at temperatures much lower than T_c ¹⁴, whereas observation of the vortex flow anti-parallel to the current in superconductivity has been hindered by the lack of suitable materials. The recently established gate-controlled BCS-BEC crossover is a promising candidate

system to investigate the anomalous vortex flow ever closer to the BEC regime. To probe the anomalous vortex motion, we focus on the Hall effect of vortices and its evolution with the carrier density.

The vortex Hall effect (VHE) is a unique transport phenomenon of superconductors, where the collective dynamics of vortices and associated magnetic fluxes produces the Hall voltage^{15,16}. The VHE has been recognized since the middle of the last century in several metallic superconductors¹⁷ and was most intensively investigated in high T_c cuprates^{15,18–22}. Though the potential importance of the BCS-BEC crossover has been discussed for cuprates^{1,23}, its impact on the Hall effect²⁴ and vortex dynamics remains elusive due to the orders competing with superconductivity such as antiferromagnetism and charge density wave²⁵. In particular, it is still unknown how the temperature-dependent sign change of the VHE, which is called Hall anomaly¹⁵, is related to the BCS-BEC crossover. In the gate-controlled Li_xZrNCl system, where no competing orders have been observed, intact effects of the BCS-BEC crossover on the VHE and vortex dynamics are expected to be unveiled by transport measurements combined with systematic control of Δ/E_F . Even comparing with highly controllable ultracold atomic gases, where transport measurements are developing^{26,27} but still challenging²⁸, Li_xZrNCl is a suitable system to systematically study the vortex dynamics in the BCS-BEC crossover.

Here we report the evolution of the VHE in the BCS-BEC crossover regime via gate-controlled superconductivity of Li_xZrNCl . We experimentally found that the Hall angle, related to vortex motion, increases with decreasing Li content x or electron density towards the crossover regime. Using the time-dependent Ginzburg-Landau (TDGL) model, we successfully explained the temperature dependence of the transverse resistivity and the x dependence of the Hall angle in a qualitative manner. The combination of experiments and theory enables us to present a comprehensive picture of vortex dynamics along the BCS-

BEC crossover. Leaving the experimental region in the crossover, the expected vortex dynamics in the BEC limit were conjectured, allowing to present a full view on the evolution of vortex dynamics. Therefore, this work shows that the Li_xZrNCl system allows for an unclouded view on the BCS-BEC crossover rendering it an ideal testbed to benchmark theories on vortex dynamics in the crossover.

Results

Experimental observation of the vortex Hall effect in Li_xZrNCl

Figure 1c, d depict side and top view, respectively, of the crystal structure of the Li-intercalated ZrNCl system (Li_xZrNCl). The host ZrNCl is a van der Waals layered material with a double honeycomb lattice composed of Zr and N, forming a band insulator. Once Li is intercalated in the van der Waals gap, one electron per Li is introduced to the ZrN conduction layer, and the system exhibits superconductivity²⁹. The Li concentration x corresponds to the carrier density. Figure 1e displays a schematic band structure of Li_xZrNCl . Electrons are introduced into the parabolic conduction bands, which are located at the \mathbf{K} and \mathbf{K}' points at the corners of the hexagonal Brillouin zone. The electronic phase diagram in the temperature T and electron density x plane is shown in Fig. 1f. The pseudo-gap state appears at rather high temperature T^* , and the superconducting transition temperature T_c exhibits a maximum at $x=0.01$, below which T_c is well scaled as $T_c/T_F=1/8$. Furthermore, the ratio of superconducting gap Δ to Fermi energy E_F increases with decreasing x ⁹. The determination of Δ and E_F , which are not specific to superconductor and cold atom systems, enables us to construct a unified experimental phase diagram of the BCS-BEC crossover (Supplementary Note 2 and Supplementary Fig. 1). This encourages us to investigate the nature of BEC superconductivity by extrapolating the trend from the BCS side.

To navigate the single-crystal ZrNCl within the BCS-BEC crossover, an intercalation-only device was employed as previously reported^{9,30}. Several doping levels were achieved (Fig. 1f, Supplementary Note 3, and Supplementary Fig. 2). The T_c data obtained in the present experiment (dark blue) agrees well with the previous results. This phase diagram allows us to correlate observed transport phenomena with the position in the crossover.

A detailed look at the transport properties is given with $x=0.0040$, 0.010 , and 0.47 in Fig. 2, which shows the longitudinal and transverse resistivities versus temperature at varying out-of-plane magnetic fields. For the lowest doping, $x=0.0040$ (Fig. 2a), superconductivity ($T_c=16.8$ K) persists even at elevated magnetic fields, and the upper critical field B_{c2} reaches 5.9 T (Supplementary Note 4 and Supplementary Fig. 3). No quantum metallic states are visible unlike the electrostatically induced monolayer or bilayer superconductivity³¹. This discrepancy is possibly because the present system is multi-layered, similarly to the bulk cuprates. The transverse resistivity ρ_{yx} (bottom) exhibits anomalous behavior. For $T>T_c$, the Hall signal is

negative ($\rho_{yx}<0$), as expected for the n-type transport in electron-doped Li_xZrNCl . For $T>T_c$, however, the transverse resistivity starts to change its sign to $\rho_{yx}>0$ and forms a peak with reducing T , which is reminiscent of the Hall anomaly¹⁵. For medium doping, $x=0.010$ (Fig. 2b), superconductivity ($T_c=15.9$ K) is less persistent at elevated fields ($B_{c2}=5.0$ T), and the Hall anomaly is observed though the magnitude is reduced. For high doping, $x=0.47$ (Fig. 2c), the system shows a sharp transition ($T_c=11.4$ K), a much lower critical field ($B_{c2}=0.8$ T), and an extremely small VHE. It is important to note that the cleanliness, i.e., the ratio of the mean free path over the coherence length has been observed to play a crucial role in the appearance of the Hall anomaly as discussed previously¹⁵. The doping dependence of the cleanliness is shown in Supplementary Fig. 4, to exclude that the observed enhancement of the Hall anomaly versus doping is largely due to a modulation of the cleanliness (see Supplementary Note 5 and Supplementary Table 1 for experimentally obtained parameters, including the mean free path and the coherence length).

The doping dependence of the VHE can be visualized by mapping the Hall coefficient $R_H (= \rho_{yx}/B)$ at different doping levels as a function of temperature and field (Fig. 3a). Blue and red areas correspond to the negative and positive R_H , respectively. The red color highlights the enhanced VHE, which appears in the low-field regime around the B_{c2} curve, where vortices are highly mobile. Here, the B_{c2} curve for each carrier density is determined by the half resistance temperature. These features strongly support that the observed Hall anomalies indeed reflect the VHE. At $x=0.47$, the VHE almost vanishes. Overall, it is evident that the magnitude and area of the VHE are increasing with decreasing doping. The maximum Hall angle Θ_H , defined at the dark red circles in each phase diagram (Fig. 3a), is summarized as a function of x in Fig. 3b. Though the temperature and field, at which Θ_H is defined (Fig. 3a), vary from sample to sample, Θ_H characterizes the strength of the VHE at each doping level. The observed x dependence of Θ_H unambiguously implies that the VHE is enhanced by reducing the carrier density, i.e., approaching the BCS-BEC crossover from the BCS side.

Theoretical modeling of the experimentally observed vortex Hall effect

To elucidate the evolution of vortex dynamics towards the BCS-BEC crossover, observed as the enhanced VHE, we calculated ρ_{xx} and ρ_{yx} using the 2D TDGL model (Eq. (1) in Methods) with the gauge invariance^{32,33}. Since the sign change of Θ_H was observed both above and below the B_{c2} curve (Fig. 3a), we focused on the dynamics in the vortex liquid state³⁴, where many interacting vortices are fluctuating in time and space¹⁶. Using a few phenomenological parameters and the E_F dependence of the gap-opening temperature T^* (Supplementary Fig. 5), which has been measured previously⁹, we obtained the longitudinal and transverse resistivities near the B_{c2} curve (Methods and

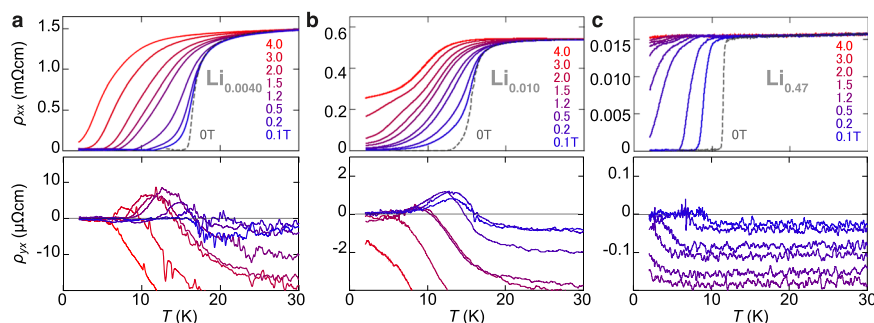


Fig. 2 | Transport properties at different doping levels x . Temperature dependence of longitudinal ρ_{xx} (top) and transverse ρ_{yx} (bottom) resistivity at varying out-of-plane fields for $x=0.0040$ **a**, $x=0.010$ **b**, and $x=0.47$ **c**. The vortex Hall

effect with sign reversal is clearly observed in **a** and **b**, whereas it is almost indiscernible in **c**. The magnitude of ρ_{yx} decreases with increasing x .

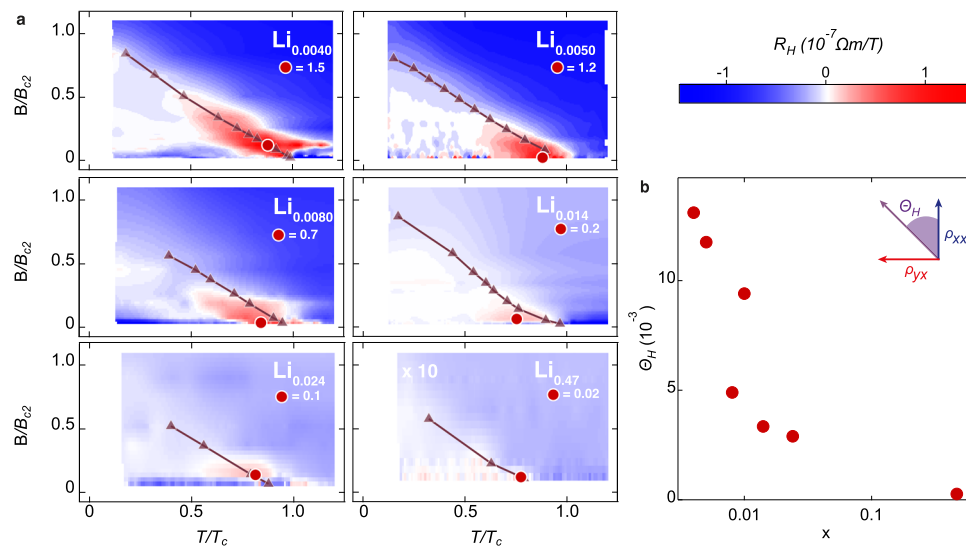


Fig. 3 | Mapping the vortex Hall effect at different doping levels. **a** Color mapping of the Hall coefficient R_H on the B-T phase diagram for different doping levels. Horizontal and vertical axes are temperature normalized by T_c and magnetic field normalized by upper critical field B_{c2} at zero temperature, respectively. The VHE is visible in the red regions with a sign change of R_H . The areas of VHE are increasing

with decreased doping. At the highest doping ($x = 0.47$), the VHE is not visible anymore. Lines and markers show the T_c (B_{c2}) superconductivity boundary determined by the half resistance. Red circles mark the maximum R_H values. **b** Doping dependence of Hall angle Θ_H . With decreasing doping, Θ_H is enhanced monotonically. In the high doping BCS regime, Θ_H almost vanishes.

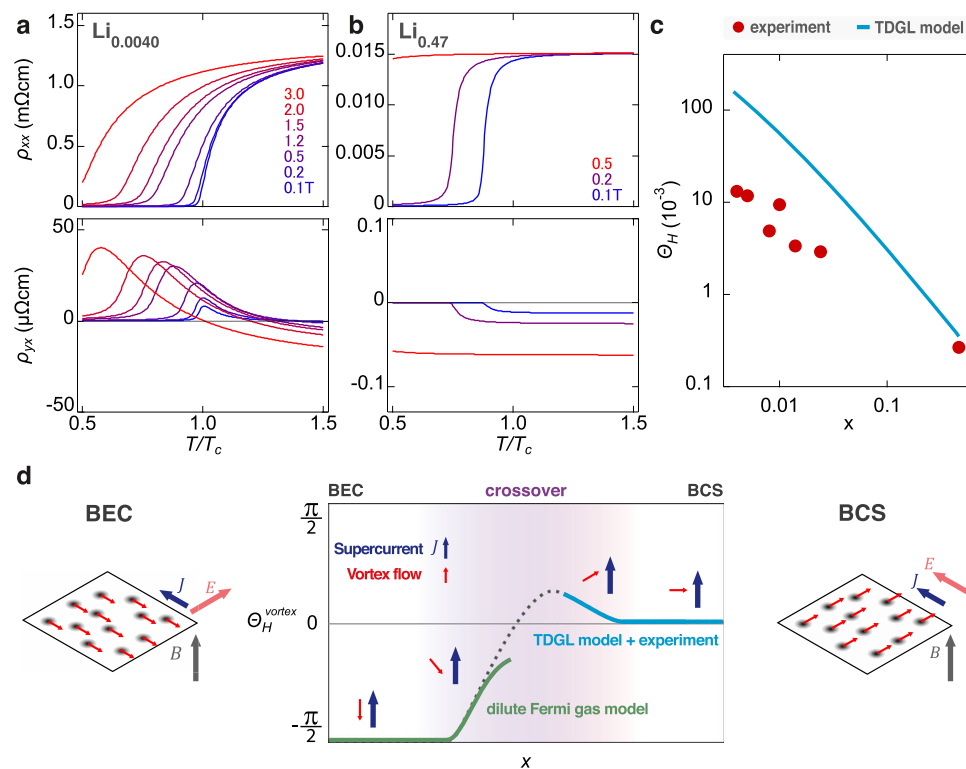


Fig. 4 | Theoretical simulations of VHE by the TDGL framework. Temperature dependence of the longitudinal resistivity ρ_{xx} (top) and the transverse resistivity ρ_{yx} (bottom) at varying out-of-plane fields for the selected doping levels $x = 0.0040$ **a** and 0.47 **b**. **c** Comparison of the theoretical and experimental doping dependence of the Hall angle Θ_H . The experimental data are taken from Fig. 3, whereas the theoretical values are obtained for lower temperatures, where the normal-state contribution is negligible (Supplementary Note 7). **d** Evolution of the vortex Hall angle Θ_H^{vortex} across the BCS-BEC crossover conjectured from the present study. The light blue curve is obtained from the experiment and TDGL model, while the light green curve is obtained theoretically using the diluted Fermi gas model.

dotted line is the interpolation between these two regimes. The blue and red arrows in the inset show the supercurrent and vortex flow, respectively. Schematics in both sides illustrate these relative motions for a set of vortices at the BEC (left) and BCS (right) limits. Here \mathbf{J} , \mathbf{E} and \mathbf{B} are the supercurrent flow, electric field induced by vortex flow, and external magnetic field, respectively. The present experiment is made around the border of the BCS and crossover regimes. It is important to note, the green curve in the BEC regime is a theoretical expectation via the dilute Fermi gas model and is beyond the experimentally supported region of the crossover and BCS regime.

Supplementary Note 6–9). We assumed a single conduction band to extract a general understanding of vortex dynamics across the BCS-BEC crossover, as independent of material details as possible.

Figure 4a, b shows the obtained temperature dependence of ρ_{xx} (top) and ρ_{yx} (bottom) for $x = 0.0040$ and 0.47 , respectively. As shown in these figures, we find a qualitative agreement with the experimentally observed temperature and field dependence of ρ_{xx} and ρ_{yx} , especially the sign change and positive peak of ρ_{yx} for $x = 0.0040$ (Fig. 2a). This agreement indicates that the peak of ρ_{yx} occurs in the vortex liquid state, without considering pinning effects. The disappearance of the clear peak in ρ_{yx} for increased x to 0.47 (Fig. 4b) also agrees well with the experiment (Fig. 2c). We have confirmed that these agreements can be obtained even if we change a parameter that is not determined from the experiments (Supplementary Figs. 6 and 7). There are still some discrepancies between experiment and theory. For instance, in the low-temperature high-field region for $x = 0.0040$, the VHE is suppressed in the experiment (Fig. 2a) but still visible in the theory (Fig. 4a). The absence of ρ_{yx} despite the finite ρ_{xx} is reminiscent of the quantum vortex liquid state in 2D superconductors³⁵. In this state, the vortex is in the liquid state by quantum fluctuation rather than thermal fluctuation^{36,37}. This quantum vortex liquid state is left to be confirmed in future studies. In particular, the development of a TDGL model including quantum fluctuations is highly anticipated.

Figure 4c compares the theoretically obtained Hall angle (Methods and Supplementary Note 7) and the experimentally observed Θ_H (Fig. 3b), which show similar trends of enhancement towards the BCS-BEC crossover. Strictly speaking, the experimental Θ_H was measured at the peak position of R_H (Fig. 3a), while the theoretical Hall angle was determined at low temperatures where the vortex contribution to the conductivity is dominant (Supplementary Note 7). Nevertheless, the similar trends in the theory and experiment suggest that the TDGL model successfully captures the evolution of the vortex dynamics and the resulting VHE towards the BCS-BEC crossover. The quantitative difference between the theory and experiment might be attributed to theoretical overestimation of the fluctuation contribution at high fields (see Supplementary Note 9).

The key to the above agreement is that the sign of the Hall angle in the vortex state is opposite to the sign of the E_F derivative of the mean-field critical temperature in the TDGL model³³ (Eq. (2) in Methods). In the BCS-BEC crossover, the mean-field critical temperature, which represents the pairing temperature^{2,3,23}, should correspond to the gap-opening temperature T^* rather than the observed critical temperature T_c . Hence, the sign of the vortex Hall angle, and thereby the occurrence of the Hall anomaly, is determined from that of dT/dE_F , which generally depends on the microscopic details of the system. Since $dT/dE_F < 0$ in Li_xZrNCl (Supplementary Fig. 5), the Hall anomaly observed as the sign change of Θ_H from negative to positive upon cooling towards the vortex state was theoretically reproduced. This situation ($dT/dE_F < 0$) can be microscopically derived from a tight binding model with a finite-range attractive interaction³⁸. The simple material nature of Li_xZrNCl seems important for the applicability of the TDGL model because, in many cuprate superconductors, the simple TDGL model is not applied possibly due to several complex features including the d -wave superconductivity¹⁹ or competing orders such as antiferromagnetism and charge density wave²⁵.

Discussion

The simple material nature of Li_xZrNCl motivated us to conjecture the evolution of vortex dynamics beyond the experimentally established region in the crossover (Fig. 4c, d light blue curve) towards the BEC limit (Fig. 4d green curve). This way, Fig. 4d displays the expected global evolution of the Hall angle Θ_H^{vortex} in the vortex state with changing the doping level x from the BEC to the BCS limit, accompanied with schematics of vortex motions in the two limits. Here we assumed that the vortex state stays liquid over all regions. In the BCS

limit, the vortex flow (thin red arrow) is perpendicular to the supercurrent (blue arrow), indicating $\Theta_H^{\text{vortex}} = 0$. The experimentally observed region (light blue line) spans from the BCS to the crossover regime, where the tilting of the vortex motion increases Θ_H as x is reduced. This behavior is supported by the theoretical expression of Θ_H^{vortex} , i.e., $\tan\Theta_H^{\text{vortex}} = \lambda/\gamma \sim O(T^*/E_F)$ (Eq. (2) in Methods and Supplementary Note 7). Here, the coefficients γ and λ represent typical times for dissipative damping and non-dissipative propagation, respectively. In other words, this equation relates the vortex Hall angle to the relative importance of dissipation (γ/λ): the vortex Hall angle is becoming smaller as the dissipation is growing larger. Thus, in the BCS region, where $T^*/E_F \simeq 0$, the dissipation is dominant ($\lambda/\gamma \simeq 0$) and the vortex Hall angle is almost zero. Furthermore, this relation suggests that $|\Theta_H^{\text{vortex}}|$ should increase as T^*/E_F increases towards the crossover region⁹. In the BEC limit as the low-doping limit, on the other hand, vortices will move anti-parallel to the supercurrent due to the dissipationless vortex core (Fig. 1a), leading to a large negative Θ_H^{vortex} . This picture in the dilute limit is also supported by the TDGL model derived from the dilute Fermi gas model with attractive interaction (Supplementary Note 11), which gives vanishing dissipation²³ ($\gamma = 0$ in Eq. (1) in Methods) and accordingly $\Theta_H^{\text{vortex}} = -\pi/2$ (green line in Fig. 4d). Thus, if one can further reduce x from the experimentally observed region, Θ_H^{vortex} is expected to form a positive peak, change its sign, and eventually approach $-\pi/2$ (black dotted line in Fig. 4d). Overall, through the BCS-BEC crossover in Li_xZrNCl , the vortex dynamics will non-monotonically evolve from dissipative motion perpendicular to the supercurrent into dissipationless motion anti-parallel to the supercurrent.

Figure 4d also provides a comprehensive view of the Hall anomaly throughout the BCS-BEC crossover, corroborated by the TDGL theory. Since Θ_H is negative (i.e., $\sigma_{yx} > 0$, see Supplementary Table 2) in the high-temperature normal state of Li_xZrNCl , the Hall anomaly, i.e., the sign reversal of Θ_H on lowering the temperature (Figs. 2 and 4a), is only expected in the intermediate BCS-BEC crossover regime where Θ_H^{vortex} is positive due to the negative sign of dT/dE_F (Fig. 4d).

In conclusion, we have systematically investigated the vortex Hall effect in the 2D BCS-BEC crossover using the recently established gate-controlled Li_xZrNCl system on the experimental side. We experimentally observed the enhancement of the Hall angle with decreasing doping within the crossover. Combined with the TDGL theory, we successfully reproduced this behavior qualitatively, and therefore present the experimentally supported evolution of vortex dynamics within the crossover. This model also allowed to conjecture the expected vortex dynamics beyond the experimental region, towards the BEC limit, unlocking a comprehensive picture of vortex dynamics throughout and beyond the BCS-BEC crossover. The simple band structure of Li_xZrNCl with absence of competing orders should be crucial to establish a clear understanding of the VHE in many superconductors including cuprates, which has been left unsolved for a long time. The presented density-controlled BCS-BEC crossover has the potential to serve as an essential platform for material exploration and investigations of the unexplored physics of superconductivity in the BEC limit, as showcased herein with the open question of vortex dynamics in the BEC limit left to be tackled experimentally.

Methods

Device fabrication

Bulk ZrNCl , prepared by a chemical vapor transport method³⁹, was exfoliated onto SiO_2/Si substrates using the scotch tape technique. The obtained single-crystalline thin flakes exhibited a thickness of ca. 10–40 nm, as determined by atomic force microscopy in tapping mode. Using electron-beam lithography (EBL) with polymethylmethacrylate (PMMA) as positive resist, Au (90 nm)/Cr (7 nm) electrodes were patterned onto a selected thin-flake in a Hall bar setup including a co-planar gate electrode in proximity. In a second EBL step

only the edges of the ZrNCl thin flakes and the gate pad were developed, leaving the Hall bar electrodes and the channel region covered with PMMA, to allow for intercalation-only operation of the device^{9,30}. For the electrolyte, LiClO₄ (Sigma Aldrich) was dissolved in polyethylene glycol (PEG, $M_w = 600$, Wako) at a Li:O (PEG) ratio of 1:20 and stored at 80 °C under vacuum. A drop of electrolyte was placed onto the device to cover both the exposed flake edges and the gate pad. A small cover glass slip was placed on top to evenly spread the electrolyte. The device was transferred into a quantum design physical property measurement system (PPMS) equipped with a rotator probe and high vacuum was applied ($<10^{-4}$ Torr) at 330 K for at least 1 h before measurement.

Transport measurements

The temperature-dependent resistance of the device at varying magnetic fields was measured in standard four-probe geometry using the PPMS combined with lock-in amplifiers (Stanford Research Systems Model SR830 DSP and Signal Recovery Model 5210) to measure current and voltage. A Keithley 2400 SMU was used to apply the gate voltage at 330 K and high vacuum. The temperature was lowered to 150 K to freeze the PEG-based electrolyte ($T_m = 288$ K), the chamber was purged with He and the Hall coefficients were measured.

TDGL model

Assuming that T^* corresponds to the mean-field critical temperature, we used the phenomenological two-dimensional (2D) time-dependent Ginzburg-Landau (TDGL) model:

$$(\gamma + i\lambda) \frac{\partial}{\partial t} \Delta(\mathbf{r}, t) = - \left[\frac{T - T^*}{T^*} + b|\Delta(\mathbf{r}, t)|^2 - \xi^2 \left(\nabla + i \frac{2\pi}{\phi_0} \mathbf{A}(\mathbf{r}) \right)^2 \right] \Delta(\mathbf{r}, t), \quad (1)$$

where b is a phenomenological parameter, ϕ_0 is the flux quantum, $\xi = (\phi_0/2\pi B_{c2})^{1/2}$ is the coherence length, and $\Delta(\mathbf{r}, t)$ is the superconducting order parameter varying in space and time. For the left-hand side, we simply used the relaxation time derived for the BCS regime⁴⁰, $\gamma = \pi/8 T^*$, and took $\lambda = -(1/2 T^*) \partial T^*/\partial E_F$, according to the gauge invariance^{32,33}. For the expression of λ , we used the mean-field critical temperature T^* instead of the observed transition temperature T_c since the derivation in Aronov et al.³³ is based only on the linear terms in the TDGL model (1). We also set the chemical potential μ to E_F in the expression of λ because $\partial T^*/\partial \mu$ presumably takes a value close to $\partial T^*/\partial E_F$ in the experimentally accessible BCS-BEC crossover region; considering the 2D Fermi gas model as a reference¹⁰, we obtain $(\partial T^*/\partial \mu)/(\partial T^*/\partial E_F) \simeq 0.99$ even when the zero-temperature superconducting gap Δ_0 is as large as $\Delta_0 = 0.4 E_F$, which is a typical value observed in Li_xZrNCl⁹ (Supplementary Note 10 and Supplementary Fig. 8). We set the vector potential as $\mathbf{A}(\mathbf{r}) = Bx\hat{y}$ in the Landau gauge, which is fixed so that the scalar potential is zero.

Calculation of longitudinal and transverse conductivities

Based on the TDGL model, after renormalizing the transition temperature from T^* to T_c (Supplementary Note 6), we applied the linear response theory within the Hartree approximation to obtain the temperature and field dependence of the longitudinal and transverse conductivities (σ_{xx}^v and σ_{yy}^v) for the vortex liquid state³⁴ (Supplementary Note 7). To calculate the resistivities (ρ_{xx} and ρ_{yy}), we introduced the normal-state longitudinal and transverse conductivities (σ_{xx}^N and σ_{yy}^N), which were obtained from the experimental data (Supplementary Table 2). For a phenomenological parameter β ($\propto b$), which represents the fluctuation interaction strength, we typically took $\beta = 10^{-4}$ – 10^{-3} , a slight change of which did not affect the qualitative behavior of ρ_{xx} or ρ_{yy} (Supplementary Note 9). In Fig. 4a, b, we show the obtained $\rho_{xx} = (\sigma_{xx}^N + \sigma_{xx}^v)/[(\sigma_{xx}^N + \sigma_{xx}^v)^2 + (\sigma_{yy}^N + \sigma_{yy}^v)^2]$ and $\rho_{yy} = -(\sigma_{yy}^N + \sigma_{yy}^v)/[(\sigma_{xx}^N + \sigma_{xx}^v)^2 + (\sigma_{yy}^N + \sigma_{yy}^v)^2]$. The Hall angle for low

enough temperatures can be obtained as (Supplementary Note 7)

$$\theta_H^{\text{vortex}} = -\arctan\left(\frac{4}{\pi} \frac{\partial T^*}{\partial E_F}\right), \quad (2)$$

which is plotted in Fig. 4c.

Data availability

The data that support the plots and other findings of this study are available from the corresponding author upon reasonable request.

References

- Chen, Q., Stajic, J., Tan, S. & Levin, K. BCS-BEC crossover: from high temperature superconductors to ultracold superfluids. *Phys. Rep.* **412**, 1–88 (2005).
- Sá de Melo, C. A. R. When fermions become bosons: pairing in ultracold gases. *Phys. Today* **61**, 45 (2008).
- Randeria, M. & Taylor, E. Crossover from Bardeen-Cooper-Schrieffer to Bose-Einstein condensation and the unitary fermi gas. *Annu. Rev. Condens. Matter Phys.* **5**, 209–232 (2014).
- Regal, C. A., Greiner, M. & Jin, D. S. Observation of resonance condensation of fermionic atom pairs. *Phys. Rev. Lett.* **92**, 040403 (2004).
- Uemura, Y. J. et al. Basic similarities among cuprate, bismuthate, organic, Chevrel-phase, and heavy-fermion superconductors shown by penetration-depth measurements. *Phys. Rev. Lett.* **66**, 2665–2668 (1991).
- Kasahara, S. et al. Field-induced superconducting phase of FeSe in the BCS-BEC cross-over. *Proc. Natl Acad. Sci. USA* **111**, 16309–16313 (2014).
- Cao, Y. et al. Unconventional superconductivity in magic-angle graphene superlattices. *Nature* **556**, 43–50 (2018).
- Park, J. M., Cao, Y., Watanabe, K., Taniguchi, T. & Jarillo-Herrero, P. Tunable strongly coupled superconductivity in magic-angle twisted trilayer graphene. *Nature* **590**, 249–255 (2021).
- Nakagawa, Y. et al. Gate-controlled BCS-BEC crossover in a two-dimensional superconductor. *Science* **372**, 190–195 (2021).
- Botelho, S. S. & Sá de Melo, C. A. R. Vortex-antivortex lattice in ultracold fermionic gases. *Phys. Rev. Lett.* **96**, 040404 (2006).
- Hazra, T., Verma, N. & Randeria, M. Bounds on the superconducting transition temperature: applications to twisted bilayer graphene and cold atoms. *Phys. Rev. X* **9**, 031049 (2019).
- Caroli, C., de Gennes, P. G. & Matricon, J. Bound Fermion states on a vortex line in a type II superconductor. *Phys. Lett.* **9**, 307–309 (1964).
- Sensarma, R., Randeria, M. & Ho, T.-L. Vortices in superfluid fermi gases through the BEC to BCS crossover. *Phys. Rev. Lett.* **96**, 090403 (2006).
- Paoletti, M. S., Fisher, M. E., Sreenivasan, K. R. & Lathrop, L. P. Velocity statistics distinguish quantum turbulence from classical turbulence. *Phys. Rev. Lett.* **101**, 154501 (2008).
- Hagen, S. J. et al. Anomalous flux-flow Hall effect: Nd_{1.85}Ce_{0.15}CuO_{4-y} and evidence for vortex dynamics. *Phys. Rev. B* **47**, 1064–1068 (1993).
- Blatter, G., Feigel'man, M. V., Geshkenbein, V. B., Larkin, A. I. & Vinokur, V. M. Vortices in high-temperature superconductors. *Rev. Mod. Phys.* **66**, 1125–1388 (1994).
- Van Beelen, H., Van Braam Houckgeest, J. P., Thomas, M. H. M., Stolk, C. & De Bruyn Ouboter, R. Some measurements on the effective resistance and the hall angle in type II superconductors. *Physica* **36**, 241–253 (1967).
- Iye, Y., Nakamura, S. & Tamegai, T. Hall effect in high temperature superconductors near T_c . *Phys. C* **159**, 616–624 (1989).
- Nagaoka, T. et al. Hall anomaly in the superconducting state of high- T_c cuprates: universality in doping dependence. *Phys. Rev. Lett.* **80**, 3594–3597 (1998).

20. Zhao, S. Y. F. et al. Sign-reversing hall effect in atomically thin high-temperature $\text{Bi}_{2-x}\text{Sr}_{1-x}\text{CaCu}_{2-x}\text{O}_{8+\delta}$ superconductors. *Phys. Rev. Lett.* **122**, 247001 (2019).
21. Auerbach, A. & Arovas, D. P. Hall anomaly and moving vortex charge in layered superconductors. *SciPost Phys.* **8**, 061 (2020).
22. Ogawa, R., Nabeshima, F., Nishizaki, T. & Maeda, A. Large Hall angle of vortex motion in high- T_c cuprate superconductors revealed by microwave flux-flow Hall effect. *Phys. Rev. B* **104**, L020503 (2021).
23. Sá de Melo, C. A. R., Randeria, M. & Engelbrecht, J. R. Crossover from BCS to Bose superconductivity: transition temperature and time-dependent Ginzburg-Landau theory. *Phys. Rev. Lett.* **71**, 3202–3205 (1993).
24. Boyack, R., Wang, X., Chen, Q. & Levin, K. Combined effects of pairing fluctuations and a pseudogap in the cuprate Hall coefficient. *Phys. Rev. B* **99**, 134504 (2019).
25. Keimer, B., Kivelson, S. A., Norman, M. R., Uchida, S. & Zaanen, J. From quantum matter to high-temperature superconductivity in copper oxides. *Nature* **518**, 179–186 (2015).
26. Anderson, R. et al. Conductivity spectrum of ultracold atoms in an optical lattice. *Phys. Rev. Lett.* **122**, 153602 (2019).
27. Xu, W., McGehee, W. R., Morong, W. N. & DeMarco, B. Bad-metal relaxation dynamics in a Fermi lattice gas. *Nat. Commun.* **10**, 1588 (2019).
28. Brown, P. T. et al. Bad metallic transport in a cold atom Fermi-Hubbard system. *Science* **363**, 379–382 (2019).
29. Kasahara, Y., Kuroki, K., Yamanaka, S. & Taguchi, Y. Unconventional superconductivity in electron-doped layered metal nitride halides MNX (M = Ti, Zr, Hf; X = Cl, Br, I). *Phys. C* **514**, 354–367 (2015).
30. Nakagawa, Y. et al. Gate-controlled low carrier density superconductors: Toward the two-dimensional BCS-BEC crossover. *Phys. Rev. B* **98**, 064512 (2018).
31. Saito, Y., Kasahara, Y., Ye, J., Iwasa, Y. & Nojima, T. Metallic ground state in an ion-gated two-dimensional superconductor. *Science* **350**, 409–413 (2015).
32. Aronov, A. G. & Rapoport, A. B. Hall effect in superconductors above T_c . *Mod. Phys. Lett. B* **6**, 1083–1088 (1992).
33. Aronov, A. G., Hikami, S. & Larkin, A. I. Gauge invariance and transport properties in superconductors above T_c . *Phys. Rev. B* **51**, 3880–3885 (1995).
34. Ullah, S. & Dorsey, A. T. Effect of fluctuations on the transport properties of type-II superconductors in a magnetic field. *Phys. Rev. B* **44**, 262 (1991).
35. Breznay, N. P. & Kapitulnik, A. Particle-hole symmetry reveals failed superconductivity in the metallic phase of two-dimensional superconducting films. *Sci. Adv.* **3**, e1700612 (2017).
36. Saito, Y., Nojima, T. & Iwasa, Y. Highly crystalline 2D superconductors. *Nat. Rev. Mater.* **2**, 16094 (2016).
37. Kapitulnik, A., Kivelson, S. A. & Spivak, B. Colloquium: anomalous metals: failed superconductors. *Rev. Mod. Phys.* **91**, 011002 (2019).
38. Shi, T., Zhang, W. & Sá de Melo, C. A. R. Density-induced BCS-Bose evolution in gated two-dimensional superconductors: The role of the interaction range in the Berezinskii-Kosterlitz-Thouless transition. *EPL* **139**, 36003 (2022).
39. Yamanaka, S., Kawaji, H., Hotehama, K.-I. & Ohashi, M. A new layer-structured nitride superconductor. Lithium-intercalated β -zirconium nitride chloride, Li_xZrNCl . *Adv. Mater.* **8**, 771–774 (1996).
40. Abrahams, E. & Tsuneto, T. Time variation of the Ginzburg-Landau order parameter. *Phys. Rev.* **152**, 416–432 (1966).

Acknowledgements

We thank T. Nojima, R. Arita, T. Nomoto, S. Hoshino, and T. Ideue for valuable discussions. This work was supported by A3 Foresight Program and JSPS KAKENHI Grant Numbers JP20K14435 and JP19H05602. M. H. was supported by Deutsche Forschungsgemeinschaft DFG, Project No. 182087777–SFB 951 and this work was conducted in the framework of the Joint Lab GEN_FAB and was supported by the HySPRINT Innovation Lab at Helmholtz-Zentrum Berlin.

Author contributions

E.L.K. and Y.I. conceived the research and designed the experimental scheme. M.H., Y.N., and Y.M.I. fabricated the devices. M.H. performed measurements and analyzed the data. Y. Kas. grew the single crystal of ZrNCl . K.A. and Y. Kat. constructed a theory and made numerical calculations. All authors discussed the results, and M.H., K.A., Y. Kat., and Y.I. wrote the manuscript.

Competing interests

The authors declare no competing interests.

Additional information

Supplementary information The online version contains supplementary material available at <https://doi.org/10.1038/s41467-022-34756-x>.

Correspondence and requests for materials should be addressed to Yoshihiro Iwasa.

Peer review information *Nature Communications* thanks the anonymous reviewers for their contribution to the peer review of this work.

Reprints and permissions information is available at <http://www.nature.com/reprints>

Publisher's note Springer Nature remains neutral with regard to jurisdictional claims in published maps and institutional affiliations.

Open Access This article is licensed under a Creative Commons Attribution 4.0 International License, which permits use, sharing, adaptation, distribution and reproduction in any medium or format, as long as you give appropriate credit to the original author(s) and the source, provide a link to the Creative Commons license, and indicate if changes were made. The images or other third party material in this article are included in the article's Creative Commons license, unless indicated otherwise in a credit line to the material. If material is not included in the article's Creative Commons license and your intended use is not permitted by statutory regulation or exceeds the permitted use, you will need to obtain permission directly from the copyright holder. To view a copy of this license, visit <http://creativecommons.org/licenses/by/4.0/>.

© The Author(s) 2022